

**CHARACTERISING MICRO-CRACKS IN
CRYSTALLINE SILICON SOLAR CELLS USING
TRANSFLECTION IMAGING**

TEO TEOW WEE

UNIVERSITI SAINS MALAYSIA

2020

**CHARACTERISING MICRO-CRACKS IN
CRYSTALLINE SILICON SOLAR CELLS USING
TRANSFLECTION IMAGING**

by

TEO TEOW WEE

**Thesis submitted in fulfilment of the requirements
for the degree of
Doctor of Philosophy**

May 2020

ACKNOWLEDGEMENTS

I would like to firstly express my sincere gratitude to my supervisor Prof. Dr. Mohd Zaid Bin Abdullah for his continuous support, for his patience, motivation, and immense knowledge. His tireless professional guidance has been invaluable during the research and writing of this thesis. One could not have imagined having a better mentor.

My sincere thanks also goes to Mr. Goon Koon Yin along with the rest of my colleagues at TT Vision Technologies Sdn. Bhd., whom provided me this opportunity to pursue this research. Without the support and resources made available to me over the years, this research would not have been possible.

I would like to extend my thanks to my fellow colleagues Dr. Zeinab Mahdavi pour for the stimulating discussions, for the experiments that we have conducted together and for the patience and critique of the initial drafts of this thesis. Mr. Lim Thai Li for the discussions, for the collaborations and for the camaraderie over the years.

I would also like to thank my family for the encouragement and for supporting me spiritually throughout this research and my life in general. Last but not least, to Ms. Wong Mei Fong for her companionship and encouragement during this research and to her I dedicate this thesis.

TABLE OF CONTENTS

	Page
ACKNOWLEDGEMENTS	ii
TABLE OF CONTENTS	iii
LIST OF TABLES	vi
LIST OF FIGURES	viii
LIST OF ABBREVIATIONS	xiii
LIST OF SYMBOLS	xv
ABSTRAK	xvi
ABSTRACT	xviii
 CHAPTER ONE: INTRODUCTION	
1.1 Background	1
1.2 Difficulties and Challenges	6
1.3 Research Objectives	9
1.4 Research Scope	10
1.5 Thesis Outline	10
 CHAPTER TWO: LITERATURE REVIEW	
2.1 Scanning Acoustic Microscopy	11
2.2 Light Beam Induced Current	14
2.3 Lock-In Thermography	16
2.4 Resonance Ultrasonic Vibration	19
2.5 Electroluminescence	21

2.6	Photoluminescence	25
2.7	Image Processing of Luminescence Images	29
2.8	Optical Transmission	33
2.9	Edge-Lighting and Vicinal Illumination.....	39
2.10	Summary	43

CHAPTER THREE: METHODOLOGY

3.1	Transflection Principle	45
3.2	System Design	50
3.2.1	Light source	51
3.2.2	Camera.....	53
3.2.3	Lens.....	56
3.3	Implementation	58
3.4	Evaluation of the System.....	59
3.5	Summary	64

CHAPTER FOUR: EXPERIMENTAL RESULTS

4.1	Silicon Wafers	65
4.1.1	Monocrystalline Slurry-Sawn Silicon Wafer	66
4.1.2	Polycrystalline Slurry-Sawn Silicon Wafer	71
4.1.3	Monocrystalline Diamond Wire-Sawn Silicon Wafer	75
4.1.4	Polycrystalline Diamond Wire-Sawn Silicon Wafer	80
4.1.5	Comparison Between Silicon Wafer Types	84
4.2	Solar Cells	87
4.2.1	Monocrystalline Solar Cell	88

4.2.2	Polycrystalline Solar Cell.....	93
4.2.3	Comparison Between Solar Cell Types	105
4.3	Limitations	108
4.4	Summary	110

CHAPTER FIVE: CONCLUSION AND FUTURE WORK

5.1	Conclusion	112
5.2	Limitations of Research	113
5.3	Recommendations for Future Work	113

REFERENCES	115
-------------------------	-----

APPENDICES

Appendix A: Optical Properties Of Silicon

Appendix B: Supplementary Solar Cell Imaging Results

LIST OF PUBLICATIONS

LIST OF TABLES

		Page
Table 1.1	Specification requirements.	9
Table 2.1	Comparison of micro-crack detection methods.	44
Table 3.1	Number of silicon wafer and solar cell samples.	60
Table 4.1	Comparison of image quality measures using images of monocrystalline slurry-sawn silicon wafers.	69
Table 4.2	Comparison of classification results using images of monocrystalline slurry-sawn silicon wafers.	70
Table 4.3	Comparison of image quality measures using images of polycrystalline slurry-sawn silicon wafers.	73
Table 4.4	Comparison of classification results using images of polycrystalline slurry-sawn silicon wafers.	74
Table 4.5	Comparison of image quality measures using images of monocrystalline diamond wire-sawn silicon wafers.	78
Table 4.6	Comparison of classification results using images of monocrystalline diamond wire-sawn silicon wafers.	79
Table 4.7	Comparison of image quality measures using images of polycrystalline diamond wire-sawn silicon wafers.	82
Table 4.8	Comparison of classification results using images of polycrystalline diamond wire-sawn silicon wafers.	83
Table 4.9	Comparison of classification accuracy of the optical transmission method and the proposed transflection system with different types of silicon wafers.	86
Table 4.10	Comparison of throughputs for inspection of solar cells.	87
Table 4.11	Comparison of image quality measures using images of monocrystalline solar cells.	89
Table 4.12	Comparison of classification results using images of monocrystalline solar cells.	92

Table 4.13	Comparison of image quality measures using images of polycrystalline solar cells.	99
Table 4.14	Comparison of classification results using images of polycrystalline solar cells.	104
Table 4.15	Comparison of classification accuracy of electroluminescence (EL), photoluminescence (PL) and the proposed transflection system with different types of solar cells.	107
Table A.1	Optical properties of silicon at 300K where λ is the wavelength, α the absorption coefficient and k the extinction coefficient (Green, 2008).	123
Table B.1	Comparison of solar cell images produced by EL and PL with the proposed transflection method.	130

LIST OF FIGURES

		Page
Figure 1.1	Illustration of a production process flow of a crystalline silicon (c-Si) based solar cell.	2
Figure 1.2	Monocrystalline silicon wafers in today's two industry standard size of $125 \times 125 \text{ mm}^2$ and $156 \times 156 \text{ mm}^2$.	2
Figure 1.3	Cropped images of slurry wire-sawn and diamond wire-sawn monocrystalline silicon wafers showing the absence and presence of saw marks respectively.	3
Figure 1.4	An example of a monocrystalline silicon wafer that has undergone anti-reflection coating (ARC) deposition.	4
Figure 1.5	An example of a fully completed polycrystalline solar cell showing the front and rear surfaces with important features annotated.	5
Figure 2.1	Schematic layout of a scanning acoustic microscopy (SAM) system showing important elements.	12
Figure 2.2	A monocrystalline solar cell acquired using SAM. The rectangle indicates the location of a micro-crack (Molina, 2012).	13
Figure 2.3	Schematic layout of a light beam induced current (LBIC) system showing important elements.	14
Figure 2.4	A monocrystalline solar cell acquired using LBIC. A micro-crack can be observed running up the cell above the micron scale bar (Colvin, 2009).	15
Figure 2.5	Schematic layout of a dark and illuminated lock-in thermography (LIT) system showing important elements.	17
Figure 2.6	A monocrystalline solar cell acquired using dark LIT. Multiple micro-cracks can be observed as hot-spots scattered throughout the solar cell (Breitenstein et al., 2011).	18
Figure 2.7	Schematic layout of a resonance ultrasonic vibration (RUV) system showing important elements. The arrow indicates the suction of the vacuum pump to keep the solar cell in place.	19

Figure 2.8	A example of an frequency response curve generated by a RUV system showing the difference between an intact solar cell and a micro-cracked one (Monastyrskyi, 2008).	20
Figure 2.9	Schematic layout of an in-line EL system showing important elements.	22
Figure 2.10	Image of a 12×6 polycrystalline solar module under EL.	23
Figure 2.11	An example of an in-line EL image of a polycrystalline solar cell. The thick horizontal black bars represents the electrical contact probes on the solar cell's busbars used to deliver an electrical current to the sample.	25
Figure 2.12	Schematic layout of an in-line PL system showing important elements.	27
Figure 2.13	Images of a polycrystalline solar cell acquired under PL and EL.	28
Figure 2.14	Image comparison of a visible light image and the PL image of a polycrystalline solar cell showing several defects, including micro-cracks.	30
Figure 2.15	Schematic layout of an optical transmission system showing important elements.	34
Figure 2.16	Cropped images of silicon wafers containing micro-cracks acquired with the optical transmission method.	35
Figure 2.17	Images of slurry wire-sawn and diamond wire-sawn monocrystalline silicon wafers acquired using the optical transmission method.	38
Figure 2.18	Schematic layout of an edge-lighting system showing important elements. The arrow indicates the direction of travel of the solar cell.	40
Figure 2.19	A polycrystalline solar cell acquired using the edge lighting system. The bright areas indicates the presence and location of multiple micro-cracks (Ortner, Gräff, Stelzl, Macherey, & Neubecker, 2013).	40
Figure 2.20	An image of a diamond wire-sawn wafer acquired using the edge-lighting system. The saw marks are highly visible in this image (Ortner et al., 2013).	41

Figure 2.21	An image of a silicon wafer acquired using the vicinal illumination strategy. The arrows indicate the position of the micro-crack (Liu et al., 2018).	42
Figure 3.1	Illustration of the transflection principle in a cross-sectional view of a solar cell showing the interaction at an intact area at scanning interval $[0, t_1]$ where the transflected light reaches the camera with no interruption.	48
Figure 3.2	Illustration of the transflection principle in a cross-sectional view of a solar cell showing the interaction at a micro-cracked area at scanning interval $[t_1, t_2]$ where the transflected light is interrupted by a crack located in between the laser and the camera.	49
Figure 3.3	Illustration of the transflection principle in a cross-sectional view of a solar cell showing the interaction at an intact area at scanning interval $[t_2, t_3]$ where the transflected light resumed transmission to the camera.	49
Figure 3.4	Schematic layout of the proposed transflection system showing important elements.	50
Figure 3.5	The variation of absorption coefficient of silicon as a function of a wavelength (Green, 2008).	52
Figure 3.6	Quantum efficiency graph of a Xenics Lynx-2048-GigE camera (“Lynx-2048-GigE Datasheet”, 2017).	55
Figure 3.7	Drawing of the transflection module using computer-aided design (CAD) showing the actual positions of each critical components of the proposed system.	58
Figure 3.8	Before and after PL image of a polycrystalline solar cell which has undergone a stress test to confirm the presence and location of micro-cracks.	61
Figure 4.1	Image of a monocrystalline slurry-sawn silicon wafer acquired using the optical transmission method. The rectangular box indicates the location of a cropped view of an area containing a micro-crack.	67
Figure 4.2	Image of the same monocrystalline slurry-sawn silicon wafer shown in Figure 4.1 acquired using the proposed transflection system showing a cross-shaped micro-crack.	68

Figure 4.3	Image of a polycrystalline slurry-sawn silicon wafer acquired using the optical transmission method. The rectangular box indicates the location of a cropped view of an area containing a micro-crack.	71
Figure 4.4	Image of the same polycrystalline slurry-sawn silicon wafer shown in Figure 4.3 acquired using the proposed transflection system showing a micro-crack.	72
Figure 4.5	Image of a monocrystalline diamond wire-sawn silicon wafer acquired using the optical transmission method. The square box indicates the location of a cropped view of an area containing a micro-crack.	76
Figure 4.6	Image of the same monocrystalline diamond wire-sawn silicon wafer shown in Figure 4.5 acquired using the proposed transflection system showing a micro-crack. The square box indicates the location of a cropped view of an area containing a micro-crack.	77
Figure 4.7	Image of a polycrystalline diamond wire-sawn silicon wafer acquired using the optical transmission method. The square boxes indicates the location of a cropped view of an area containing a micro-crack.	80
Figure 4.8	Image of the same polycrystalline diamond wire-sawn silicon wafer shown in Figure 4.7 acquired using the proposed transflection system showing some micro-cracks.	81
Figure 4.9	Bar graph of average energy values in images produced by the optical transmission method and the proposed transflection system from different types of silicon wafers.	85
Figure 4.10	Bar graph of average standard deviation in images produced by the optical transmission method and the proposed transflection system from different types of silicon wafers.	85
Figure 4.11	Image of a monocrystalline solar cell acquired under EL.	90
Figure 4.12	Image of a monocrystalline solar cell acquired under PL.	91
Figure 4.13	Image of the same monocrystalline solar cell as in Figure 4.11 and Figure 4.12 acquired using the proposed transflection system.	91
Figure 4.14	Image of an intact polycrystalline solar cell acquired under EL.	94

Figure 4.15	Image of an intact polycrystalline solar cell acquired under PL.	94
Figure 4.16	3D plot of grey scale values of the EL image in Figure 4.14.	96
Figure 4.17	3D plot of grey scale values of the PL image in Figure 4.15.	96
Figure 4.18	Image of an intact polycrystalline solar cell acquired using the proposed transflection system.	98
Figure 4.19	3D plot of grey scale values of the transflection image shown in Figure 4.18.	98
Figure 4.20	Image of a polycrystalline solar cell acquired using the PL imaging method. The square box indicates the location of a cropped view of an area with a micro-crack. The dashed line across the micro-crack marks the location of a scan line used to plot the grey scale value profile shown in Figure 4.21.	101
Figure 4.21	Grey scale value profile across a line in the PL image shown in Figure 4.20 .	101
Figure 4.22	Image of a polycrystalline solar cell acquired using the proposed transflection method. The square box indicates the location of a cropped view of an area with a micro-crack. The dashed line across the micro-crack marks the location of a scan line used to plot the grey scale value profile shown in Figure 4.23.	103
Figure 4.23	Grey scale value profile across a line in the image shown in Figure 4.22.	103
Figure 4.24	Bar graph of average energy values in images produced by EL, PL and the proposed transflection system from both types of solar cells.	106
Figure 4.25	Bar graph of average standard deviation values in images produced by EL, PL and the proposed transflection system from both types of solar cells.	106
Figure 4.26	Example of a shadow produced by a micro-crack which is oriented in parallel and perpendicular to the laser line.	109
Figure 4.27	Close up view of a bottom edge of a silicon wafer showing a narrow band lacking illumination in an image acquired by the proposed system.	110

LIST OF ABBREVIATIONS

ARC	Anti-Reflection Coating
c-Si	Crystalline Silicon
CAD	Computer-Aided Design
CCD	Charge-Coupled Device
CMOS	Complementary Metal-Oxide Semiconductor
DC	Direct Current
EL	Electroluminescence
FN	False Negative
FP	False Positive
FOV	Field Of View
GLCM	Grey-Level Co-occurrence Matrix
InGaAs	Indium Gallium Arsenide
IR	Infrared
LBIC	Light Beam Induced Current
LED	Light-Emitting Diode
LIT	Lock-In Thermography
NIR	Near-Infrared
PL	Photoluminescence
PV	Photovoltaics

RUV	Resonance Ultrasonic Vibration
SAM	Scanning Acoustic Microscopy
SVM	Support Vector Machine
SWIR	Short-Wavelength Infrared
TN	True Negative
TP	True Positive
UPH	Units Per Hour
WD	Working Distance

LIST OF SYMBOLS

f	Focal Length
h	Dimension Measure
i	Horizontal Pixel Coordinate
j	Vertical Pixel Coordinate
k	Extinction Coefficient
p	Entry of a Matrix
t	Time
v	Velocity
x	Data Vector
F_p	Pixels Number
L	Line Frequency
N	Size Vector
R_f	Required Resolution
R_i	Image Resolution
R_s	Spatial Resolution
V	Grey Scale Value
α	Absorption Coefficient
λ	Wavelength
σ	Standard Deviation

PENCIRIAN KERETAKAN-MIKRO SEL SOLAR SILIKON KRISTAL DENGAN PENGIMEJAN TRANSFLAKSI

ABSTRAK

Kaedah terkini seperti elektropendarkilau dan fotopendarkilau biasanya digunakan untuk mengesan keretakan-mikro di dalam sel solar memandangkan kecacatan ini tidak dapat dikesan dengan mata kasar. Tetapi, imej yang dihasilkan oleh teknik-teknik tersebut didapati sukar untuk diproses akibat gangguan ciri-ciri lain yang mirip dengan keretakan-mikro sehingga menyebabkan kejituan klasifikasi yang amat rendah. Teknik-teknik lain seperti kaedah penghantaran cahaya optik hanya boleh digunakan untuk wafer silikon. Kaedah ini juga menghadapi masalah kejituan yang rendah akibat gangguan kesan gergaji yang berpunca dari perubahan teknik gergaji wafer yang baru diperkenalkan. Untuk menyelesaikan masalah ini, sistem pengesanan keretakan-mikro sel solar yang berdasarkan prinsip transflaksi cahaya telah dicadangkan. Dengan sistem ini, sinaran cahaya akan memasuki wafer silikon atau sel solar dan seterusnya disebarkan luas ke pelbagai arah. Sebaran cahaya ini akan menyebabkan kawasan persekitaran dalam wafer silikon atau sel solar diterangi dari bawah permukaan. Keretakan-mikro yang berada di sepanjang laluan transmisi cahaya akan menghalang transmisi seterusnya. Halangan ini akan menyebabkan perubahan keamatan yang merupakan bayangan keretakan-mikro pada imej yang dihasilkan. Transmisi cahaya ini tidak dipengaruhi oleh kesan gergaji, sempadan butiran, kehelan, calar kosmetik dan lain-lain. Oleh itu, keretakan-mikro adalah jauh lebih jelas dalam imej yang dihasilkan sekiranya ia dibandingkan dengan imej-imej dari kaedah-kaedah lain yang sedia ada. Justeru, keretakan-mikro amat mudah untuk dibezakan dan kaedah ini boleh mencatat kejituan klasifikasi melebihi 96.7% berbanding dengan kaedah-kaedah lain yang sedia ada. Selain itu, sis-

tem yang dicadangkan ini juga didapati boleh mencatat kelajuan sekurang-kurangnya 3600 unit sejam. Oleh itu, kaedah yang dicadangkan ini adalah amat sesuai untuk digunakan sebagai alat pemeriksaan atas saluran berkelajuan tinggi hari ini.

CHARACTERISING MICRO-CRACKS IN CRYSTALLINE SILICON SOLAR CELLS USING TRANSFLECTION IMAGING

ABSTRACT

Existing state-of-the-art methods such as electroluminescence and photoluminescence are commonly used today to detect micro-cracks in solar cells as they are typically invisible to naked human eyes. However, images that these tools produce was found to be difficult to process as they contain many unwanted noises that are indistinguishable to micro-cracks, therefore resulting in low detection accuracy. Other techniques such as the optical transmission method only works at the silicon wafer stage. Moreover, this method was also found to be prone to error due to interference from saw marks caused by recent changes to the wafer sawing technique. Solving this problem has lead to a design of an imaging system based on light transflection principle. In this case, an incident light enters a silicon wafer or a solar cell and is diffusely scattered in multiple directions. As a result, an area in the vicinity of the incident light is illuminated from beneath the surface. The presence of micro-cracks along the transmission path of the transflected light causes an abrupt change in the illumination intensity, thereby creating a shadow representation of the defect. This transmission of light however is not influenced by saw marks, grain boundaries, dislocations, cosmetic scratches, etc. Therefore, micro-cracks in images produced by the proposed method are distinctively visible compared to images acquired by existing methods. On average, the proposed method resulted in classification accuracy of at least 96.7%, which is significantly higher than existing methods. The system was also found to be capable of throughputs of at least 3600 units per hour. Therefore, such a method is ideally suited as an in-line inspection tool in today's high throughout production environment.

CHAPTER ONE

INTRODUCTION

1.1 Background

As the world faces the threat of climate change, clean renewable energy is becoming an increasingly important source of energy sought by many countries. Among the various types of clean renewable energy available today, photovoltaics (PV) in recent years has evolved from a niche market of specialised applications with limited capacity to a viable mainstream energy source contributing to a growing slice of the market. However, as with all renewable energy sources, cost is a determining factor for deployments as it would have to compete with relatively cheaper conventional energy sources like fossil fuel and coal.

A large majority of the PV deployments today are largely driven by crystalline silicon (c-Si) based solar cells (Philipps & Warmuth, 2019). These c-Si solar cells can be divided to two distinct types based on the raw materials used, either monocrystalline or polycrystalline silicon. Monocrystalline solar cells are made using wafers cut from an ingot grown from a single silicon crystallite, while polycrystalline solar cells are made using wafers cut from an ingot grown with multiple crystallites. Monocrystalline solar cells are typically more efficient compared to polycrystalline solar cells, however, among the two types; polycrystalline solar cells command the majority of the market share due to its lower material and manufacturing costs (Bruton, 2002; Philipps & Warmuth, 2019).

A standard production flow shared by both monocrystalline and polycrystalline based solar cells are shown in Figure 1.1. The production process starts with the production of silicon wafers cut from silicon ingots. The technology used to cut these silicon blocks used to be based on the slurry wire-sawing technique where silicon ingots are cut by a steel wire on which abrasive slurry is poured (Bhagavat, Prasad, & Kao, 2000; Möller, 2004; Möller, 2006). This produces relatively thin layers of silicon wafers typically in today's industry standard size of $125 \times 125 \text{ mm}^2$ and $156 \times 156 \text{ mm}^2$. Examples of such silicon wafers are shown in Figure 1.2.

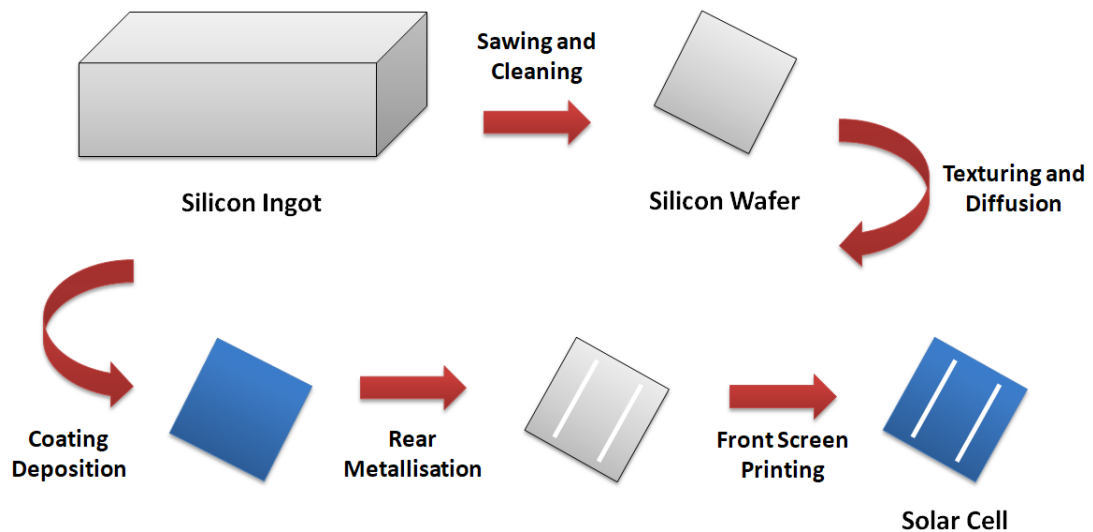


Figure 1.1: Illustration of a production process flow of a c-Si based solar cell.

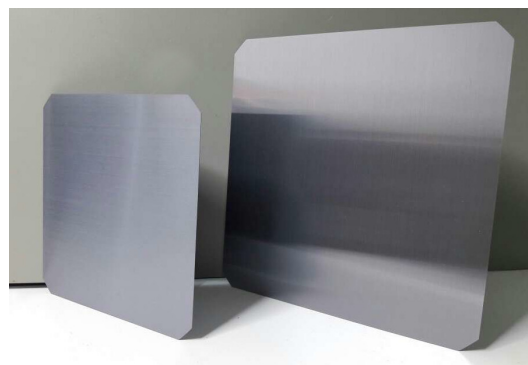


Figure 1.2: Monocrystalline silicon wafers in today's two industry standard size of $125 \times 125 \text{ mm}^2$ and $156 \times 156 \text{ mm}^2$.

In recent years, the slurry wire-sawing technique to produce silicon wafers are being gradually replaced by a new sawing technique in the form of diamond-plated wire-sawing (Tso, Yan, & Lo, 2006; Watanabe et al., 2010). In this new technique, the same saw as slurry wire-sawing is used, however the steel wire is replaced by a type of wire containing diamond particles and the abrasive slurry is replaced by a cooling liquid (Bidiville, Wasmer, Kraft, & Ballif, 2009). As the abrasive particles are bound to the wire instead of the slurry, diamond wire-sawing is much faster and has a lower wire wearing rate. This sawing technique also results in lower kerf loss and is regarded to be a more environmentally friendly method (Kumar & Melkote, 2018). The diamond wire-sawing technique however produces silicon wafers with grooves or saw marks on the surface which corresponds to the direction of the wire during sawing. Slurry-sawn wafers in comparison do not exhibit such saw marks. A cropped comparison of a slurry wire-sawn wafer and a diamond wire-sawn wafer is shown in Figure 1.3. These saw marks do have marginal impact to the performance of a solar cell (Bidiville et al., 2009; Seigneur, Schneller, Shiradkar, & Schoenfeld, 2016), nevertheless the efficiency of the technique in terms of speed and cost savings far outweighs the drawbacks.



(a) Slurry wire-sawn wafer



(b) Diamond wire-sawn wafer

Figure 1.3: Cropped images of slurry wire-sawn and diamond wire-sawn monocrystalline silicon wafers showing the absence and presence of saw marks respectively.

Silicon wafers can contribute up to 40% of the overall cost to manufacture a solar cell (Bruton, 2002). Therefore, significant cost reductions can be achieved by using less of the material by moving to thinner wafers. However, due to the brittle nature of silicon, c-Si based solar cells are now even more prone to micro-cracks as much thinner wafers are used. Micro-cracked silicon wafers have to be removed from a production line before they are further processed to avoid further material wastages.

Silicon wafers will further undergo processes such as texturing on its front surface to reduce reflectance and to improve light trapping (Papet et al., 2006), and the diffusion process to form the $p-n$ junctions in the c-Si (Deutsch et al., 1981). An anti-reflection coating (ARC) layer will also be deposited to the front surface to reduce reflectance. This results in the blue coloured tint typically observed on the front surface of c-Si solar cells (Zhao & Green, 1991). An example of a silicon wafer that has undergone ARC deposition is shown in Figure 1.4. Due to the relatively soft materials used in the ARC layer, this layer is vulnerable to scratches. However, these scratches are cosmetic in nature and do not significantly affect the anti-reflection properties of the layer. Therefore, they are not considered as a major defect to most manufacturers.

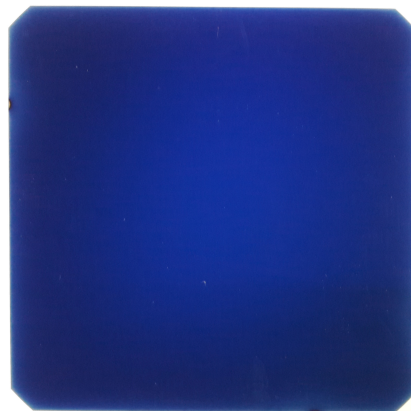


Figure 1.4: An example of a monocrystalline silicon wafer that has undergone ARC deposition.

These partially complete solar cells will undergo additional processes such as the rear metallisation and screen printing of the electrical contacts to form the busbars and cell fingers of a fully completed c-Si solar cell. An example of a fully completed solar cell is shown in Figure 1.5.

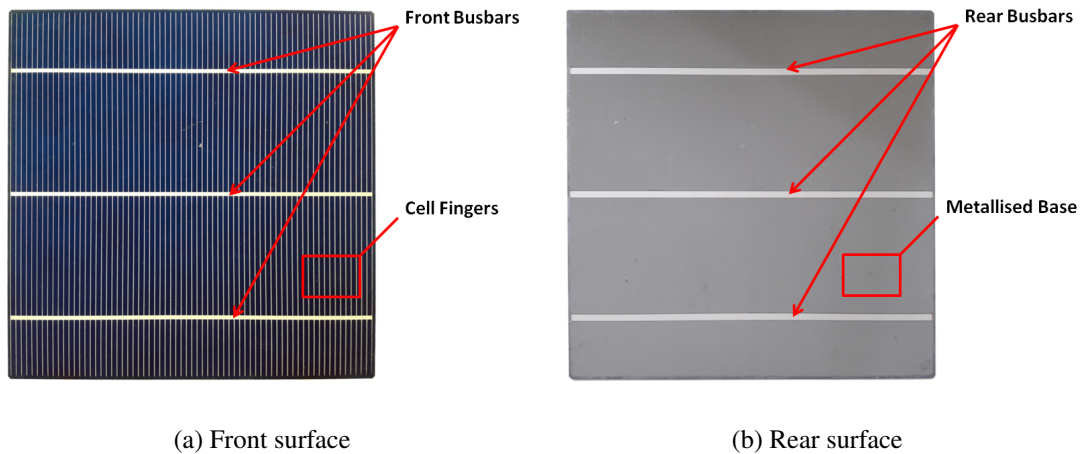


Figure 1.5: An example of a fully completed polycrystalline solar cell showing the front and rear surfaces with important features annotated.

Each manufacturing process stage exerts physical stresses upon the solar cell. These physical stresses in combination with rough handling between processes and issues with the underlying material can also potentially cause micro-cracks (Berghold, Geipel, Frank, Zemen, & Pingel, 2009; Brun & Melkote, 2009; Molina, 2012). These micro-cracks not only weaken the structural integrity of a solar cell and affecting its energy conversion efficiency, it can also become a potential source of a fire hazard as such a defect can cause thermal ‘hot-spots’ to occur (Köntges, Kunze, Kajari-Schröder, Breitenmoser, & Bjørneklett, 2011; Simon & Meyer, 2010).

As solar cells are expected to have a lifetime of 25 years or more, micro-cracks which are left undetected would pose a major warranty issue to manufacturers as the cost of replacements can be very expensive. As such, it is essential to detect and identify micro-cracks throughout the manufacturing process to remove defective materials as soon as it occurs.

1.2 Difficulties and Challenges

Micro-cracks in c-Si based solar cells are defined as cracks with size physically smaller than 30 μm in width (Chiou & Liu, 2011), therefore they are typically difficult to identify due to their relatively small size. Furthermore, this defect is often embedded within the layers of a solar cell making them invisible to naked human eyes. Solar cell manufacturers would be required to deploy specialised tools, either automated with machine vision or semi-automated with a human inspector to detect such defects as a solar cell is being manufactured on a production line.

Today's c-Si solar cells are being manufactured on production lines with typical throughputs of 3600 units per hour (UPH) or higher. For such a high throughput production environment, automated inspection systems would be a prerequisite as the required inspection speed will exceed the capability and accuracy of a human inspector. Several imaging methods are being used today to inspect micro-cracks, and the method employed would depend on the manufacturing process stage of the solar cell.

Inspections for micro-cracks during production are typically split into two distinct stages due to the different inspection methodologies used; the silicon wafer stage and the finished solar cell stage (Israil, Anwar, & Abdullah, 2013). Inspections on silicon

wafers are performed at the very early stage of production where the incoming silicon wafers are inspected for micro-cracks before further work are performed on them such as the printing of the electrical contacts at the front and rear surfaces. Meanwhile, finished solar cells are naturally inspected at the very end. Inspections on these two distinct stages require very different inspection methodologies as the material composition and physical features of the solar cell changes throughout the various stages of the manufacturing process.

Silicon wafers at the very beginning of a solar cell production process are regularly inspected using the industry standard near-infrared (NIR) backlight transmission technique, or also known as the optical transmission method (Chiou & Liu, 2011; Ko, Liu, & Lin, 2013). This technique has high throughputs of up to 3600 UPH with detection accuracy of 99.8% for micro-cracks (Mahdavi-pour, Teo, & Abdullah, 2015). However, due to recent industry wide switch from the slurry wire based sawing to the diamond wire-sawing technique in silicon wafer production; the optical transmission method became vulnerable to the presence of saw marks. Saw marks did not exist when silicon wafers are cut using the previous slurry wire-sawing technique. These saw marks can share similar characteristics as micro-cracks in images produced by the optical transmission method. As a result, high false positive rates of up to 50% can occur (Mahdavi-pour et al., 2015).

Completed solar cells near the end of the production process are regularly inspected using the electroluminescence (EL) (Fuyuki, Kondo, Yamazaki, Takahashi, & Uraoka, 2005) or the photoluminescence (PL) (Trupke, Bardos, Schubert, & Warta, 2006) imaging method. These imaging methods are typically limited to a throughput of 2400 UPH

due to physical contact requirements for EL and stationary image acquisitions for PL. Although widely used in industry, images produced by EL and PL are difficult to process even to an experienced human inspector. This is due to the presence of many unwanted noises caused by grain boundaries, dislocations and other abnormalities that share similar features as micro-cracks, making the task of defect identification difficult. As such, attempts to automate inspections using image processing require some sophisticated image processing algorithms. Nevertheless, despite much advancements in image processing in this field in recent years, the unwanted noises can still cause high false positive rates of up to 20% (Anwar & Abdullah, 2014).

The presence of unwanted noises in images produced by existing micro-crack imaging techniques is currently the leading cause of high false positives. This resulted in a significant loss of yield to c-Si solar cell manufacturers as non-defective silicon wafers and solar cells are regularly discarded due to incorrect detections. Furthermore, these unwanted noises can also cause false negatives as they can obscure actual defects from detection.

Therefore, to overcome the shortcomings of existing methods, a micro-crack characterisation approach that can produce images with relatively low amount of noise can help to improve the reliability of micro-crack detection. Such improvements will increase today's c-Si solar cell production yields which will lead to production cost savings.

1.3 Research Objectives

Due to limitations with existing micro-crack characterisation techniques in regards to interference from unwanted noises, this research has the following objectives:

1. To investigate and develop a new imaging technique to characterise micro-cracks in crystalline silicon wafers and solar cells.
2. To evaluate the capability of the new proposed technique in characterising micro-cracks in crystalline silicon wafers and solar cells.

In addition to the research objectives listed above, the new imaging system is required to be dimensionally compact to meet the specifications as shown in Table 1.1. These specifications are designed for practical integration into existing c-Si solar cell production lines.

Table 1.1: Specification requirements.

Criteria	Requirement
Sample type	Monocrystalline & polycrystalline solar cells / silicon wafers
Sample size	$156 \times 156 \text{ mm}^2$
Distinguishable micro-crack length	$\geq 1 \text{ mm}$
Throughput rate	$\geq 3600 \text{ UPH}$
Maximum system dimensions	$450 \times 450 \times 450 \text{ mm}^3$

1.4 Research Scope

A c-Si solar cell undergoes multiple production stages, many of which are proprietary processes unique to each manufacturer. Samples of these in-process solar cells are very difficult to obtain as these are considered trade secrets by most manufacturers.

Therefore, this research will be limited to the development of a practical in-line solution used to perform inspection of micro-cracks in the two common stages shared with all manufacturers; the silicon wafers at the early stages, and the finished product, a fully completed c-Si solar cell. Samples from both of these stages used in this research are available in the open market.

1.5 Thesis Outline

This thesis is arranged into five chapters. In addition to this chapter, Chapter 2 reviews a selection of existing relevant works in regards to micro-crack characterisation in silicon wafers and solar cells. Chapter 3 introduces the theoretical background and the design and implementation of a proposed imaging system based on light transfection. Procedures to evaluate the proposed system are also discussed here. Evaluation results of the proposed transfection system in comparison with existing commercially available methods are qualitatively and quantitatively presented in Chapter 4. Finally, Chapter 5 concludes the findings of this research.

CHAPTER TWO

LITERATURE REVIEW

In this chapter, a review of a selection of established methods to perform micro-crack inspections in c-Si solar cells and wafers commonly used in the industry today is presented. In literature, several methods are popularly used to detect micro-cracks in c-Si solar cells and wafers; they include scanning acoustic microscopy (SAM) discussed in Section 2.1, light beam induced current (LBIC) in Section 2.2, lock-in thermography (LIT) in Section 2.3, resonance ultrasonic vibration (RUV) in Section 2.4, EL imaging, PL imaging in Section 2.5 to Section 2.7 and variations of the optical transmission and light scattering methods in Section 2.8 and Section 2.9 respectively. Each of these methods has their own unique advantages and disadvantages and these are elaborated in each method's respective sections. Section 2.10 then summarises the discussions of this chapter.

2.1 Scanning Acoustic Microscopy

SAM is one of the earliest methods used to detect micro-cracks in silicon wafers and solar cells. First introduced by Lemons and Quate (1974), the technique uses an acoustic scanning tool to detect differences in the echo of a frequency due to micro-cracks. This is a method commonly used in the semiconductor industry to detect voids and cracks in various materials (Connor, Fine, Achenbach, & Seniw, 1998; Knauss, Zhai, Briggs, & Martin, 1995).

The method works by generating an ultrasound acoustic wave that has high penetration depth by a piezoelectric transducer that converts electrical signals into acoustic waves and vice versa during the detection stage. The acoustic waves can then be focused to a precise location within a silicon wafer or a solar cell and its echo recorded. As the acoustic wave propagates through the sample, it may be scattered, absorbed or reflected at interfaces, including those created by micro-cracks. The presence of a micro-crack interface will change the amplitude of the echo and would therefore indicate the presence of the defect. Figure 2.1 shows the working concept of a SAM system.

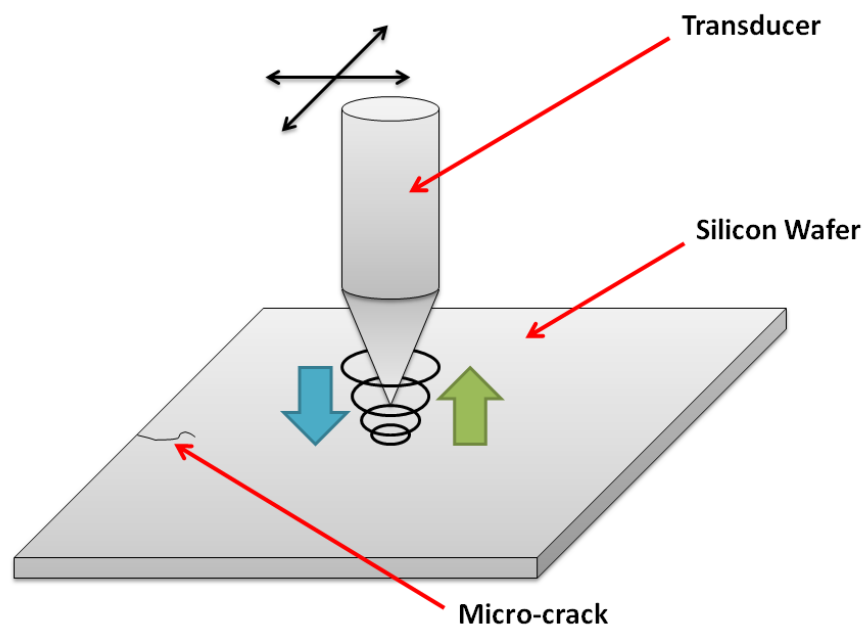


Figure 2.1: Schematic layout of a SAM system showing important elements.

SAM is capable of inspections at very high spatial resolutions of up to $5 \mu\text{m}$ at a single point (Saijo, 2009). However, to inspect an entire surface of a silicon wafer or solar cell, the transducer will be required to make multiple readings at that resolution while being scanned across the entire surface of the sample. The recorded amplitude of

the echo can then be converted into grey scale values to create an image representation of the inspected sample. An example of a monocrystalline solar cell acquired using SAM is shown in Figure 2.2.

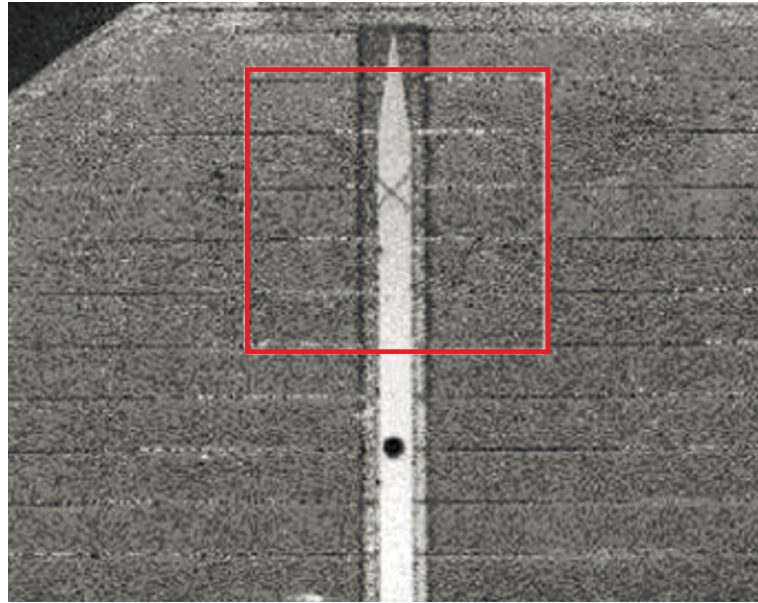


Figure 2.2: A monocrystalline solar cell acquired using SAM. The rectangle indicates the location of a micro-crack (Molina, 2012).

The process to scan the entire sample however can be very time consuming. Inspection time would depend on the sample size and the required resolution. It can take up to 15 minutes to scan a $20 \times 20 \text{ mm}^2$ solar cell with a resolution of $20 \mu\text{m}$ (Dressler et al., 2015). At this rate, it will take more than an hour to inspect a typical $156 \times 156 \text{ mm}^2$ solar cell. This is far too slow to be useful for a high throughput production environment. Furthermore, the inspected sample has to be immersed in a liquid medium to enable subsurface detection of cracks (Quate, Atalar, & Wickramasinghe, 1979). Such immersion into a liquid medium is impractical to be implemented in today's dry based production lines. As such, SAM is more commonly used as a lab based material analysis tool.

2.2 Light Beam Induced Current

Introduced by Donolato (1983), the LBIC technique is also used for characterisation of solar cells at very high spatial resolutions with reported spatial resolutions of $<100\ \mu\text{m}$ (Krebs & Jørgensen, 2014). LBIC works by focusing and scanning a high intensity light beam (usually a laser) over the surface of a solar cell, thus creating electron-hole pairs in the semiconductor causing a direct current (DC) current to flow, which in turn is measured using a current measuring device. Figure 2.3 shows a typical layout of a LBIC system.

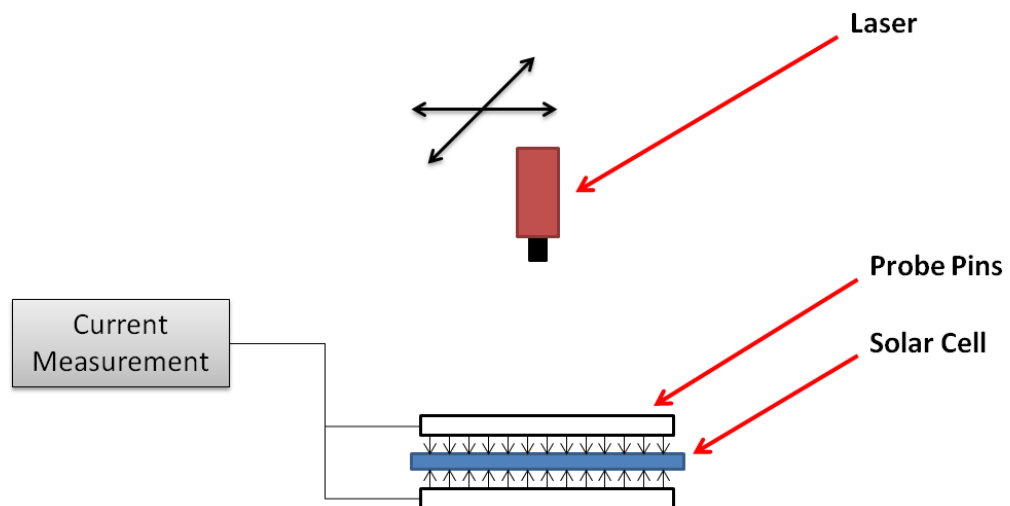


Figure 2.3: Schematic layout of a LBIC system showing important elements.

The measured current are then recorded and converted into grey scale values to create an image representation of the inspected sample. A large change in the generated current would indicate that the solar cell contains some form of anomaly. This includes micro-cracks, recombination defects and impurities. An example of a monocrystalline solar cell acquired using LBIC is shown in Figure 2.4.

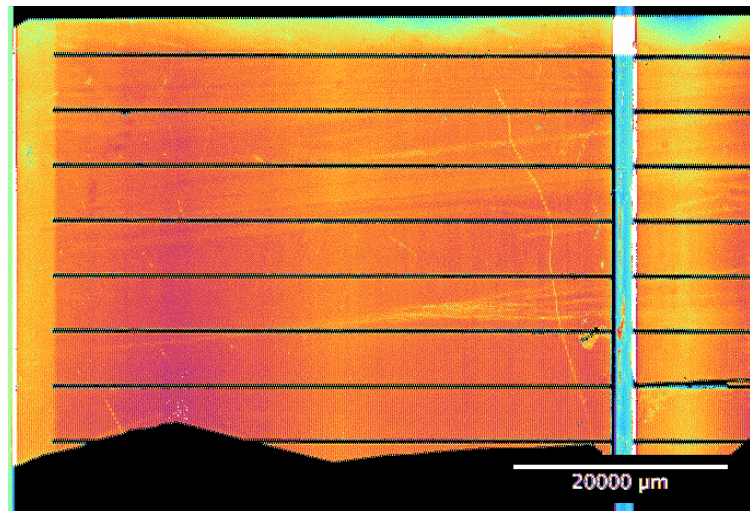


Figure 2.4: A monocrystalline solar cell acquired using LBIC. A micro-crack can be observed running up the cell above the micron scale bar (Colvin, 2009).

However, like SAM, the process to scan an entire surface of solar cell is also very time consuming. This is due to the many data points the method requires - typically about 350,000 data points for $100 \times 100 \text{ mm}^2$ is required to map an entire surface of a solar cell (Carstensen, Popkirov, Bahr, & Föll, 2003). Although Acciarri, Binetti, Racz, Pizzini, and Agostinelli (2002) developed an in-line LBIC system by reducing the number of data points to a minimum and thus sacrificing the spatial resolution of the system, inspections can still take up to 3 s for a $100 \times 100 \text{ mm}^2$ solar cell, making it impractical for today's high throughput production environment.

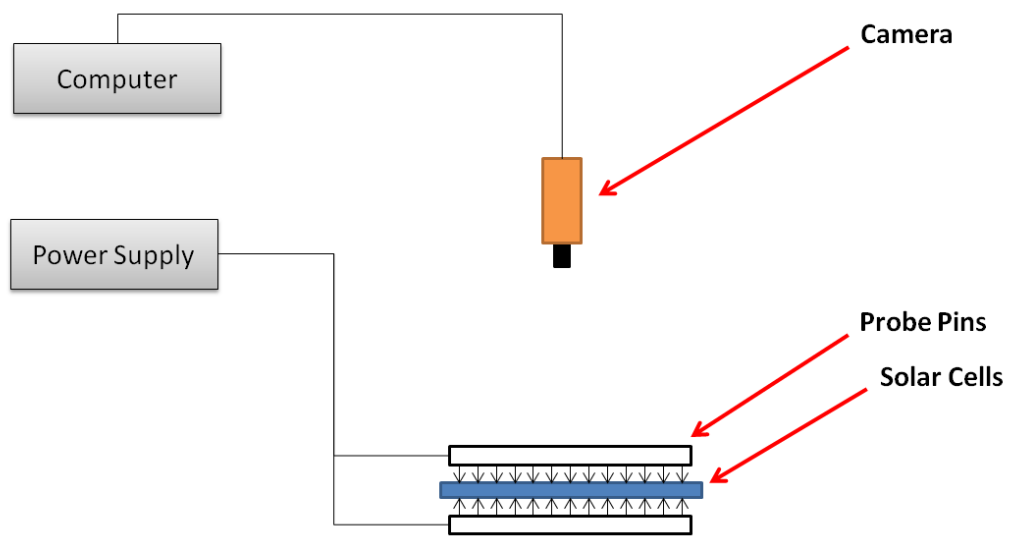
Furthermore, as the method requires physical contact for the necessary electrical current measurements, it would only work with fully completed solar cells. Nevertheless, LBIC is still a very useful characterisation tool used in many research labs today.

2.3 Lock-In Thermography

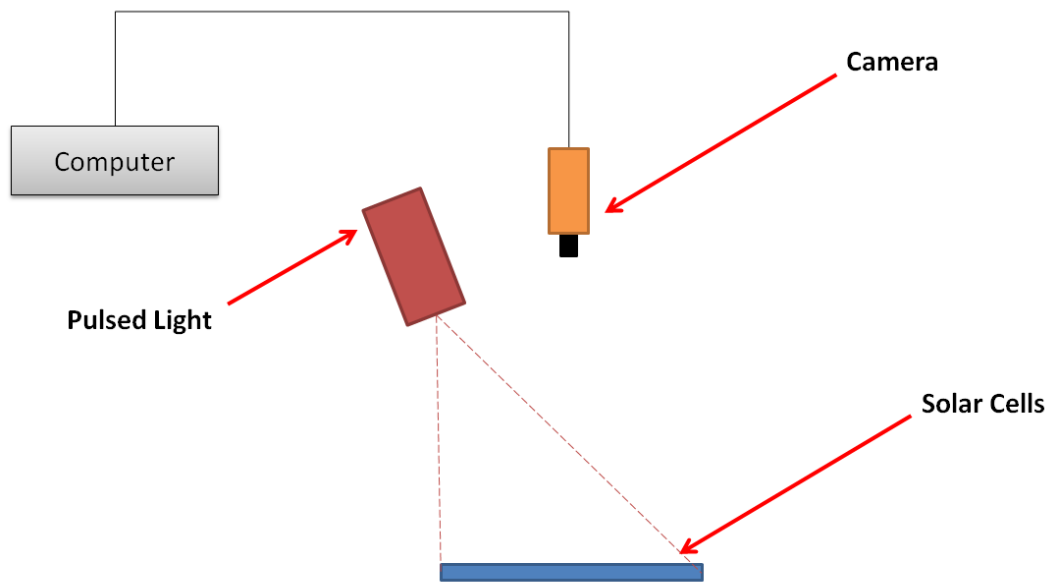
The LIT technique first introduced by Kuo, Ahmed, Jin, and Thomas (1989) was further refined by Breitenstein, Langenkamp, Lang, and Schirmacher (2001) as a dedicated characterisation tool for c-Si solar cells. This is a technique that works by imaging thermal hot-spots created by defects such as micro-cracks.

There are two techniques to perform LIT, the dark LIT and illuminated LIT. The former works by applying an electrical current in reverse bias to a solar cell by means of electrical contact probes to the front and rear busbars of a solar cell to concentrate the current in shunts, while the latter uses a light source to do the same (Breitenstein, Warta, Schubert, & Langenkamp, 2018). Illuminated LIT could work with silicon wafers and solar cells, while dark LIT will only work with fully completed solar cells as electrical contacts are required. Figure 2.5 shows typical layouts of both LIT systems.

The concentration of currents in shunts such as those created by micro-cracks will generate thermal hot-spots. Thermal signatures of these hot-spots are then imaged by a thermal imaging camera in a LIT system to generate a heat map of the solar cell. Micro-cracks can then be identified from the hot-spots in the acquired image. An example of an image acquired using dark LIT is shown in Figure 2.6.



(a) Dark LIT.



(b) Illuminated LIT.

Figure 2.5: Schematic layout of a dark and illuminated LIT system showing important elements.

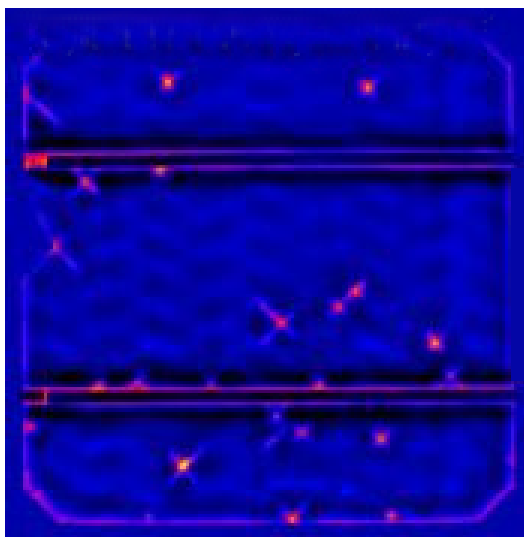


Figure 2.6: A monocrystalline solar cell acquired using dark LIT. Multiple micro-cracks can be observed as hot-spots scattered throughout the solar cell (Breitenstein et al., 2011).

Although the pixel resolution of modern and state-of-the-art thermal imaging cameras is well below 1 mm, the actual resolution of LIT systems is several magnitudes higher than this value (Breitenstein et al., 2018). This is due to the high lateral heat conductivity of silicon which causes thermal blurring and hence degrades the spatial resolution of these systems. Therefore it is challenging to detect smaller sized micro-cracks (Breitenstein et al., 2011).

Furthermore, heat conduction takes time, therefore LIT has a relatively long data acquisition time which can take up to several minutes up tens of minutes per sample (Breitenstein, 2013). As a result, LIT is impractical for in-line inspections due to its throughput limitations.

2.4 Resonance Ultrasonic Vibration

The RUV method introduced by Belyaev et al. (2006) on the other hand relies on the changes in resonance frequency due to the physical variation in silicon wafers and solar cells caused by micro-cracks. Unlike SAM, LBIC, and LIT, RUV has a relatively short data acquisition time of ≤ 2 s that can potentially meet some in-line production throughput speeds.

A RUV system requires a controlled delivery of ultrasonic vibrations into a silicon wafer or solar cell using an ultrasonic transducer. To couple the transducer to the sample, a vacuum pump is used to keep the silicon wafer or solar cell in place. The transducer frequency is swept in the range from 20 kHz to 100 kHz. This vibration propagates into the sample and is detected using an ultrasonic probe located at the edge of the sample to generate a resonance frequency response curve. Figure 2.7 shows a typical layout of a RUV system.

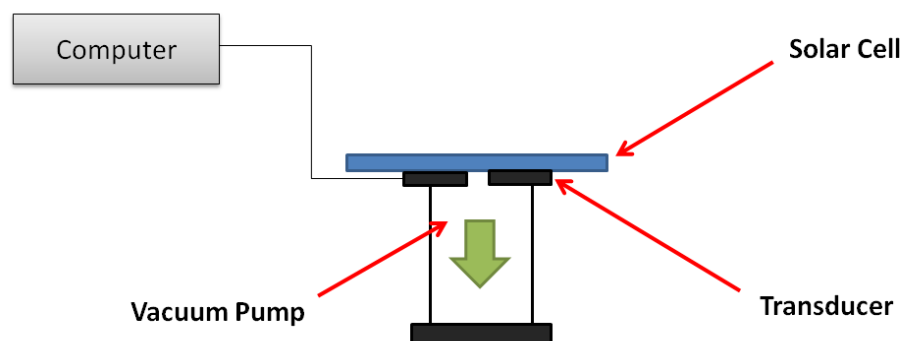


Figure 2.7: Schematic layout of a RUV system showing important elements. The arrow indicates the suction of the vacuum pump to keep the solar cell in place.

The resonance frequency response curve can then be analysed to detect defects. In the case of micro-cracks, three rejection criteria are used (Monastyrskiy, 2008): (1) shift of the peak position downward; (2) increase of the bandwidth, and (3) reduction of the amplitude. Figure 2.8 shows an example of such a frequency response curve.

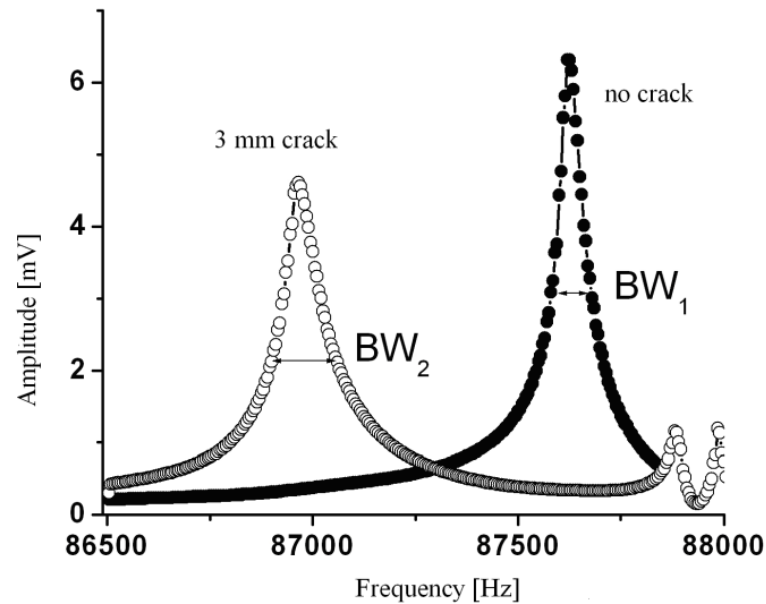


Figure 2.8: A example of an frequency response curve generated by a RUV system showing the difference between an intact solar cell and a micro-cracked one (Monastyrskiy, 2008).

The RUV method however suffers from a high degree of variation in resonance frequency even on similarly processed silicon wafers or solar cells with the same shape and size, leading to high false detections of up to 9% (Monastyrskiy, 2008). The variations are even more significant for polycrystalline silicon wafers and solar cells due to the differences in resonance frequencies between the multiple crystallites. As a result, RUV does not work for such types of silicon wafers and solar cells.

Furthermore, unlike imaging techniques, the RUV method would not be able to reveal the characteristics and the exact location of the micro-crack on a defective sample as it would only be able to indicate the absence or presence of the defect based on the analysis of the resonance frequency response curve. This would be a disadvantage as the characteristics and location data is important to solar cell manufacturers for defect cause analysis.

2.5 Electroluminescence

One such method that is capable of revealing the characteristics and location of micro-cracks, and yet has the inspection speed that may meet in-line production throughput demands is EL. First introduced by Fuyuki et al. (2005), this technique produces luminescence from a solar cell by exciting electrons into the conduction band. As a result of electron-hole recombination using an electrical current, excess energy will be created and dissipated with an emission of light. Disruptions to the electron-hole recombination such as those caused by micro-cracks will cause the defective area to emit little to no EL. Since its introduction, EL has become an essential characterisation tool, not just for micro-cracks, but also for the electrical, optical and material properties of solar cells (Bothe et al., 2006).

An EL system consists of a NIR sensitive camera and electrical probes connected to a power supply. Figure 2.9 shows a layout of an in-line EL system where a camera is placed directly above a probe station. The probe station would contain a set of pogo pins to deliver an electrical current to the front and rear busbars of a solar cell. A forward bias current would be applied to the solar cell at around 30 – 35 mA/cm²

and an open circuit voltage of 0.55 – 0.65 V, which would correspond to the typical short circuit current under 1 sun solar irradiation (Fuyuki, Kondo, Kaji, Ogane, & Takahashi, 2007). Typical EL emission of light peaks at about 1150 nm in the NIR spectrum (Fuyuki & Kitiyanan, 2009).

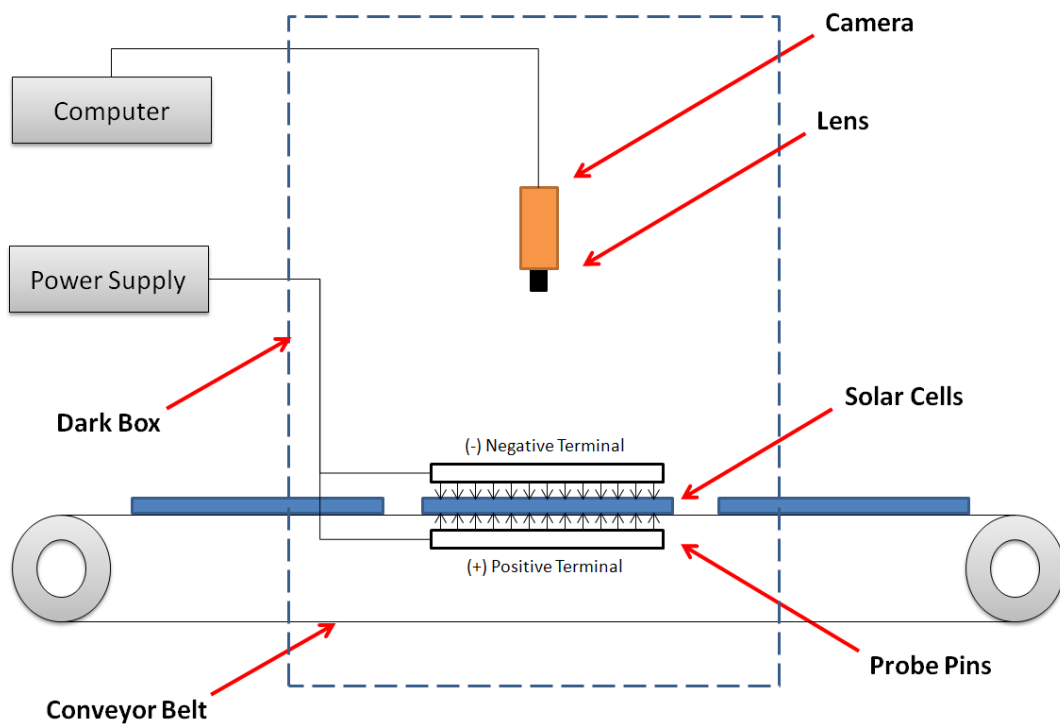


Figure 2.9: Schematic layout of an in-line EL system showing important elements.

Due to the physical contact requirements to deliver an electrical current, the EL method can only be performed on fully completed solar cells and not silicon wafers. It is also mechanically complicated to probe each individual solar cell on a production line as an accurate probing action may limit a production line's throughput speed; while at the same time risks causing micro-cracks in the first place due to the physical stresses imparted upon the solar cell during inspection. Today's in-line EL systems

typically has a throughput of 2400 UPH such as the MCV-2400EL module produced by this research's industrial partner TT Vision Technologies Sdn. Bhd., Malaysia.

Nevertheless, EL is widely used for solar module inspections, since all the required electrical contacts are already in place. A solar module consists of a grid of solar cells with their electrical contacts already stringed and soldered together. An example of a 12×6 polycrystalline solar module imaged under EL is shown in Figure 2.10.

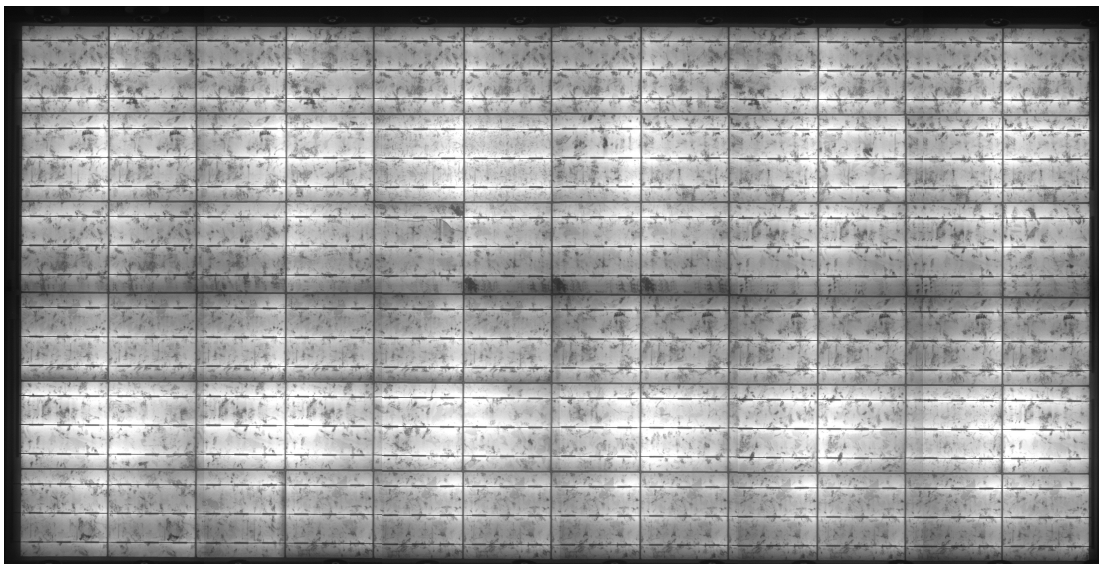


Figure 2.10: Image of a 12×6 polycrystalline solar module under EL.

EL is capable of showing a myriad of defects such as micro-cracks, electrical connectivity issues, inactive areas, contaminations, anomalous material compositions, dislocation clusters and so forth; defects which are not visible to naked human eyes, therefore it has become an important characterisation tool. However, the capability of EL to highlight multiple characteristics of solar cells also makes the task of identifying micro-cracks more challenging, especially for polycrystalline solar cells. Poly-

crystalline solar cells are made from multiple silicon crystallites, and each crystallite would emit slightly different EL intensity and would therefore produce a random heterogeneous texture in EL images. Material impurity, grain boundaries and dislocation clusters would also produce random noises in EL images that share similar textural features as micro-cracks, making the task of defect identification difficult even to experienced human inspectors. Further discussion on the difficulties in processing EL images are described in Section 2.7.

An in-line inspection using the EL method would also require contact probes which can obscure areas near the busbars of the solar cell, creating a 'blind-spot' as potential micro-cracks under the probes cannot be visualised by the camera. An example of an EL image showing the busbar areas being obscured by the contact probes is shown in Figure 2.11. This issue can potentially become more significant in the future as solar cell designs are evolving to feature more busbars to shorten the effective finger length in order to minimise resistance loss and material usage (Braun, Micard, & Hahn, 2012).